Acta Materialia 234 (2022) 118010

Contents lists available at ScienceDirect

Acta Materialia

journal homepage: www.elsevier.com/locate/actamat

Atomic structure and electrical/ionic activity of antiphase boundary in $CH_3NH_3PbI_3$

Shulin Chen [a,b,#], Changwei Wu [c,d,#], Qiuyu Shang [e,#], Zhetong Liu [a], Caili He [f], Wenke Zhou [g], Jinjin Zhao [f], Jingmin Zhang [a], Junlei Qi [h], Qing Zhang [e,*], Xiao Wang [c,*], Jiangyu Li [c,i,*], Peng Gao [a,j,k,l,*]

[a] Electron Microscopy Laboratory, School of Physics, Peking University, Beijing 100871, China
[b] KAUST Catalysis Center (KCC), Division of Physical Sciences and Engineering, King Abdullah University of Science and Technology (KAUST), Thuwal, 23955-6900, Saudi Arabia
[c] Shenzhen Key Laboratory of Nanobiomechanics, Shenzhen Institute of Advanced Technology, Chinese Academy of Sciences, Shenzhen 518055, China
[d] Guangdong Provincial Key Laboratory of Electronic Functional Materials and Devices, Huizhou University, Huizhou 516001, Guangdong, P. R. China
[e] School of Materials Science and Engineering, Peking University, Beijing 100871, China
[f] School of Materials Science and Engineering, School of Mechanical Engineering, Shijiazhuang Tiedao University, Shijiazhuang, 050043, China
[g] Army Engineering University of PLA, State Key Laboratory for Disaster Prevention & Mitigation of Explosion & Impact, Nanjing, 210007, China
[h] State Key Laboratory of Advanced Welding and Joining, Harbin Institute of Technology, Harbin 150001, China
[i] Guangdong Provincial Key Laboratory of Functional Oxide Materials and Devices, Department of Materials Science and Engineering, Southern University of Science and Technology, Shenzhen 518055, China
[j] International Center for Quantum Materials, School of Physics, Peking University, Beijing 100871, China
[k] Collaborative Innovation Center of Quantum Matter, Beijing 100871, China
[l] Interdisciplinary Institute of Light-Element Quantum Materials and Research Center for Light-Element Advanced Materials, Peking University, Beijing 100871, China

ARTICLE INFO

Article history:
Received 5 March 2022
Revised 28 April 2022
Accepted 4 May 2022
Available online 5 May 2022

Keywords:
Organic-inorganic hybrid perovskites
Low dose imaging
Antiphase boundary
Electrical activity
Ion migration

ABSTRACT

Defects in organic-inorganic hybrid perovskites (OIHPs) greatly influence their optoelectronic properties. Identification and better understanding of defects existing in OIHPs is an essential step towards fabricating high-performance perovskite solar cells. However, directly visualizing the defects is still a challenge for OIHPs due to their sensitivity during electron microscopy characterizations. Here, by using low dose scanning transmission electron microscopy techniques, we observe the common existence of antiphase boundary (APB) in $CH_3NH_3PbI_3$ ($MAPbI_3$), resolve its atomic structure, and correlate it to the electrical/ionic activities and structural instabilities. Such an APB is caused by the half-unit-cell shift of $[PbI_6]^{4-}$ octahedron along the [100]/[010] direction, leading to the transformation from corner-sharing $[PbI_6]^{4-}$ octahedron in bulk $MAPbI_3$ into edge-sharing ones at the APB. Based on the identified atomic-scale configuration, we further carry out density functional theory calculations and reveal that the APB in $MAPbI_3$ repels both electrons and holes while serves as a fast ion-migration channel, causing a rapid decomposition into PbI_2 that is detrimental to optoelectronic performance. These findings provide valuable insights into the relationships between structures and optoelectronic properties of OIHPs and suggest that controlling the APB is essential for their stability.

1. Introduction

Organic-inorganic hybrid perovskites (OIHPs) hold great promise for the next-generation solar cells because of their impressive power conversion efficiency (PCE) and facile cost-effective processing route [1–4]. During the synthesis of OIHPs, the comparably low temperature and fast nucleation and crystallization from the solution inevitably cause unintentional point and planar defects [5]. The defects density (10^{16}–10^{17} cm^{-3}) in a solution deposited $CH_3NH_3PbI_3$ ($MAPbI_3$) film is much higher than that in a single crystal $MAPbI_3$ (10^{10}–10^{11} cm^{-3}) [6]. These defects greatly influence the electrical and ionic activities and are considered to be responsible for the hysteresis, charge trapping and scattering, and ion migration in OIHPs, further causing inferior performance and instability [6]. For example, the point defects such as cation antistites and Pb interstitials in OIHPs cause deep-level defects and

* Corresponding authors.
# These authors contributed equally: Shulin Chen, Changwei Wu, Qiuyu Shang

https://doi.org/10.1016/j.actamat.2022.118010
1359-6454/

nonradiative recombination centers [7], which trap charges and limit the photovoltaic performance. Li et al. reported that the PCE and the lifetime of the carrier are deteriorated with the increased density of twinning and stacking faults in perovskite solar cells (PSCs) [5]. Moreover, the defect density at the grain boundary (GB) is several orders of magnitude higher than that inside of the grain [8] while GB is generally considered as a shortcut for ion migration [9], leading to large hysteresis [10]. Moreover, some suggest that GB is electrically benign and facilitates charge separation and collection [11,12] while others propose that GB plays as the nonradiative recombination center and deteriorates the device performance [8].

Besides the point defects, twinning, stacking faults, and GB, antiphase boundary (APB) also commonly exists in the PSCs. Indeed, previous studies reported APB usually presents unique electrical and ionic properties that are absent in the bulk [13–15]. In oxide perovskites, atomic-resolved transmission electron microscopy (TEM) images show that APB displays an antipolar phase in $La_{2/3}Sr_{1/3}MnO_3$ and induces a giant piezoelectric coefficient in $NaNbO_3$ [16]. In transition metal dichalcogenides, APB acts as a faceted metallic wire to facilitate electron transport [17] while it repels both electrons and holes in all-inorganic perovskite [18]. Reducing the APB defects in $GaInP_2$ films significantly increases the minority carrier lifetime and eliminates rapid carrier recombination [19]. APB also has a great impact on ion migration in functional devices. Kaufman et al. revealed that APB migration is a fundamental diffusion mechanism in sodium layered oxide with quite low kinetic barriers [20]. Also, APB provides additional diffusion channels for lithium-ion migration in Li_xCoO_2 [21]. Heisig et al. find that APB constitutes fast cation diffusion in $SrTiO_3$ memristive devices and decreases the diffusion barrier of Sr^{2+} from 4.0 eV to 1.3 eV [22], and thus $SrTiO_3$ memristive devices with intentionally induced APB requires no forming steps [23]. Considering the great impact of APB on electrical and ionic activities, which are closely related to the optoelectronic performance of PSCs, it is necessary to identify the atomic structure of APB in OIHPs and reveal how it influences the optoelectronic properties.

So far, there have been few reports of the atomic structure of APB in OIHPs, let alone its impact on the electrical and ionic activity. This is mainly because APB features a half-unit-cell shift of registry with respect to two adjacent regions. Although TEM proves to be one of the most powerful tools to study APB [24], OIHPs are extremely sensitive to electron beam illumination [25,26], making it challenging to observe atomic-scale structures of APB. Recently, Rothmann et al. have successfully observed the atomic structure, boundary, and defects of $CH(NH_2)_2PbI_3$ ($FAPbI_3$) by low dose scanning TEM (STEM) techniques [27]. In this work, we adopted similar low-dose STEM techniques to resolve the atomic structure of APB in $MAPbI_3$ and then clarified its impact on electrical and ionic activities via density functional theory (DFT) calculations. Atomic-scale images show that APB is composed of the edge-shared $[PbI_6]^{4-}$ octahedron and prefers to propagate along the [100] and [010] directions. Based on such an atomic structure, the effect of APB in $MAPbI_3$ on the electrical/ionic activity is clarified by DFT calculations. We find that while APB in $MAPbI_3$ does not introduce any deep-level defects and repels both electrons and holes, the diffusion barriers of $CH_3NH_3^+$ (MA^+), Pb^{2+}, and I^- are lowered at the APB compared to that in the bulk $MAPbI_3$. These suggest that APB provides a fast ion-migration channel, facilitating a more facile decomposition of $MAPbI_3$ into PbI_2. These findings provide atomic-scale insights into the structure of APB in $MAPbI_3$ and clarify the influence of APB on electrical/ionic activity, which enhances our understanding of the correlations between structures and optoelectronic properties.

2. Materials and methods

2.1. $MAPbI_3$ synthesis

$MAPbI_3$ nanocrystals were bought from Xiamen Luman Technology Co., Ltd. $MAPbI_3$ films were grown directly on the ultrathin carbon-coated copper TEM grids, as previously reported [28]. Specifically, the precursor solution was prepared by mixing 99.5% pure methlammonium iodide (MAI) and 99.999% lead iodide (PbI_2) in dimethylformamide to get a 45 wt.% solution. Then the obtained precursor solution was deposited on ultrathin carbon-coated copper grids (300 mesh) by spin coating at 6000 r.p.m. for 70 s. During this process, 50 µL chlorobenzene was dropped on the spinning substrate after 30 s, followed by annealing at 100 °C for 10 min. Thus the $MAPbI_3$ film can be obtained [29].

2.2. $CsPbBr_3$ synthesis

CsBr (0.4 mmol) and $PbBr_2$ (0.4 mmol) were dissolved in dimethylformamide (10 mL). 1 mL oleic acid and 0.5 mL oleylamine were added into the precursor solution. After, 1 mL precursor solution was added into 10 mL toluene quickly with strong stirring. Then 1 mL solution was mixed with 4 mL methyl acetate, and centrifuged at 8000 r.p.m. for 4 min, followed by dissolving into 1 mL toluene to get $CsPbBr_3$ crystals [30].

2.3. Characterization

The selected area electron diffraction (SAED) patterns and STEM images were conducted at an aberration-corrected FEI (Titan Cubed Themis G2) operated at 300 kV. SAED images were obtained at 1 e Å^{-2} s^{-1}. STEM images of $MAPbI_3$ were acquired at a current of 1 pA, a convergence semi-angle of 21.4 mrad, and a collection semi-angle snap in the range of 25−153 mrad, which allows the efficient imaging of low-Z elements [31]. The specific imaging condition was summarized in Table S1. The dose rate in STEM mode is estimated by dividing the screen current by the area of the raster [32]. To reduce the electron beam damage, the spherical aberration and focus were adjusted away from imaged areas. Most grains in $MAPbI_3$ thin film are grown with the [001] direction that is vertical to the thin carbon substrate (Fig. 1). In this case, most STEM images present atomic resolution along the [001] direction without adjusting the zone axis. Electron energy loss spectroscopy (EELS) spectra were obtained at 300 keV, 30 pA, with the convergence semi-angle 30 mrad and collection semi-angle 5.9 mrad. HRTEM images were acquired by a DDEC camera using electron-counting mode with the dose fractionation function. The drift was corrected by DigitalMicrograph software. The original image stack contains 40 subframes in 4 s. Atomistic models were constructed by VESTA software. STEM images in Fig. 2c, Fig. 3a, b, Fig. 4, Fig. S5, Fig. S8, Fig. S10 and Fig. S11 have been filtered by Gaussian blur and Fig. 4 is stacking with 5 images. The original images were provided in supplementary materials. The area of each grain in $MAPbI_3$ film was acquired by the imageJ software. Multislice simulations of the STEM were performed by using QSTEM software simulation (https://www.physics.hu-berlin.de/en/sem/software/software_qstem) according to the experimental parameters.

2.4. Density functional theory calculations

Our first-principles calculations were carried out within the framework of DFT as implemented in the Vienna ab initio simulation package code [33,34]. The electron-ion interactions were described by the projector augmented-wave method [35]. The electron exchange-correlation was treated by a generalized gradient

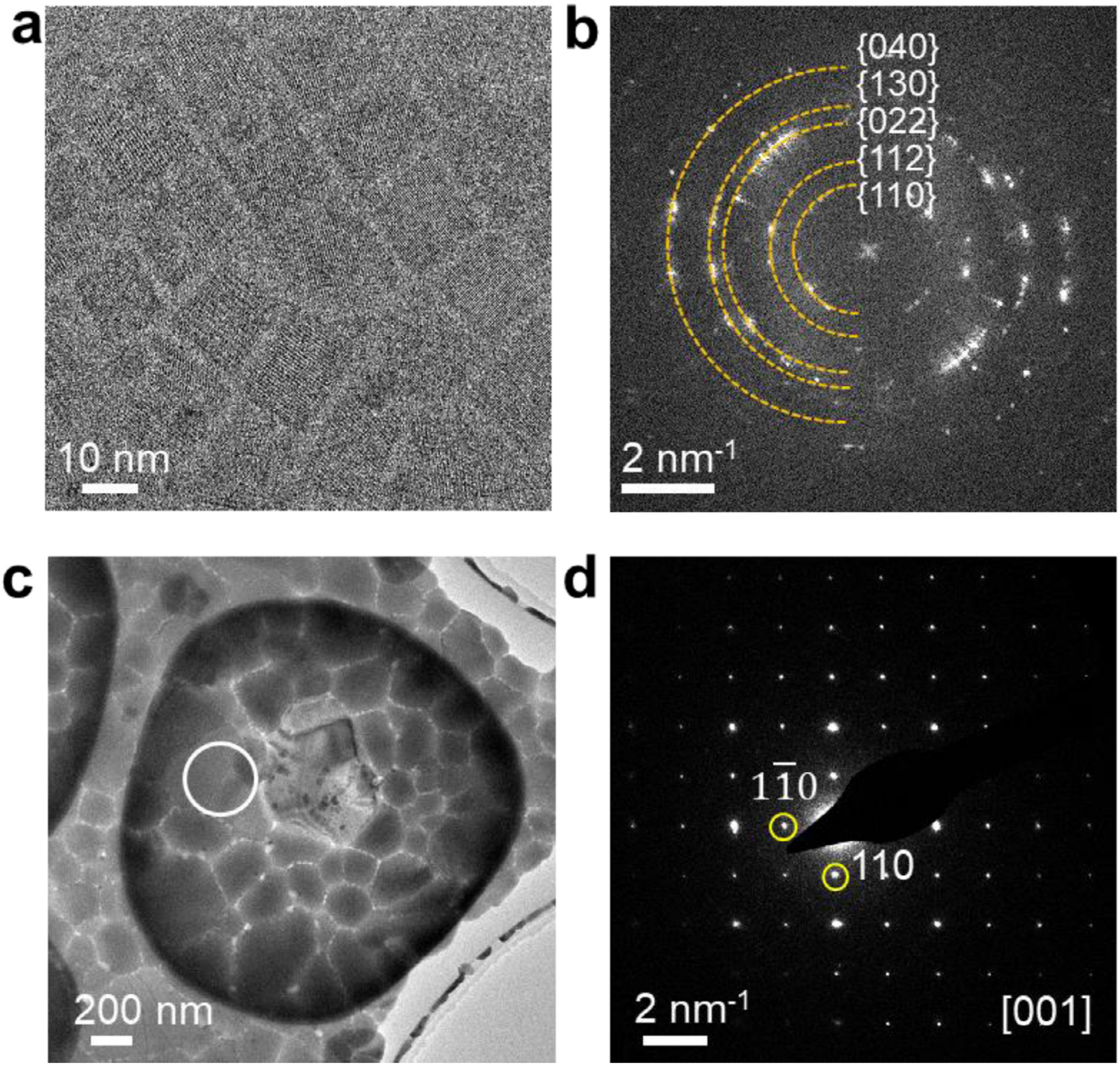

Fig. 1. Morphology and crystallinity of $MAPbI_3$ nanoparticles and film. a TEM image showing nano-particles with size 10–20 nm. b The corresponding FFT pattern. The dashed half-circles indicate the {110}, {112}, {022}, {130}, and {004} planes of $MAPbI_3$. c TEM image of polycrystalline $MAPbI_3$ film. d Electron diffraction pattern along the [001] direction of $MAPbI_3$, acquired from the region highlighted by the white circle in c.

approximation with Perdew-Bruke-Ernzerhof functional [36]. The kinetic cutoff energy was set as 500 eV for the Kohn-Sham orbitals being expanded on the plane-wave basis. The supercell size of APB was repeated periodically along the [100] direction. The atomic positions and lattice constants were fully optimized with a conjugate gradient algorithm until the Hellman-Feynman force on each atom is less than 0.01 eV/Å [37]. The Monkhorst-Pack k-point meshes were sampled as $9 \times 9 \times 7$ and $3 \times 9 \times 7$ for the $MAPbI_3$ and APB, respectively [38]. The minimum energy pathways of ions migration were determined through the climbing image nudged elastic band method [39] based on the interatomic forces and total energies acquired from DFT calculations. We performed the Ab initio molecular dynamic (AIMD) simulation in a canonical ensemble. The Brillouin zone was sampled at the Γ point and the time step of the AIMD simulation is 1 fs.

3. Results and discussion

Nanocrystal and polycrystal $MAPbI_3$ are chosen to investigate the atomic structures of the defects in $MAPbI_3$. Fig. 1a shows the TEM image of nanocrystal $MAPbI_3$ with size about 10–20 nm and the corresponding fast Fourier transform (FFT) pattern presents the {110}, {112}, {022}, {130} and {040} planes of $MAPbI_3$ (Fig. 1b). Polycrystalline $MAPbI_3$ thin film was directly grown on the ultrathin carbon-coated TEM copper grids. Each domain size is around 100–300 nm (Fig. 1c) with good crystallinity (Fig. 1d). The polycrystalline $MAPbI_3$ thin film thickness is estimated to be 30–45 nm based on EELS measurements (Fig. S2).

Since $MAPbI_3$ is sensitive to the electron beam [40–42], low-dose imaging techniques including direct-detection electron-counting (DDEC) camera and low-dose scanning transmission electron microscopy (STEM) were used to obtain the atomic structures of $MAPbI_3$ (Fig. 2). Fig. 2a shows high resolution TEM (HRTEM) image acquired at a dose of 28.2 e $Å^{-2}$ by DDEC camera from nanocrystal $MAPbI_3$. Based on our previous study by comparing the HRTEM simulation (Fig. S3) and structural features of $MAPbI_3$ [43], the yellow, blue and white circles are identified to be Pb^{2+}/I^-, I^- and MA^+ columns respectively. Yet there are many MA^+ vacancies as highlighted by the yellow squares in Fig. 2a under electron beam illumination [43], thus the corresponding FFT pattern shows superstructure spots (Fig. 2b). In contrast, the acquired STEM image of polycrystal $MAPbI_3$ shows more visible atomic columns along the [001] direction. The yellow, blue and white circles present Pb^{2+}/I^-, I^- and MA^+ columns according to the Z-contrast feature of STEM imaging. By comparing the STEM simulation of $MAPbI_3$ (Fig. S4) with the experimental image (Fig. 2c), some MA^+ vacan-

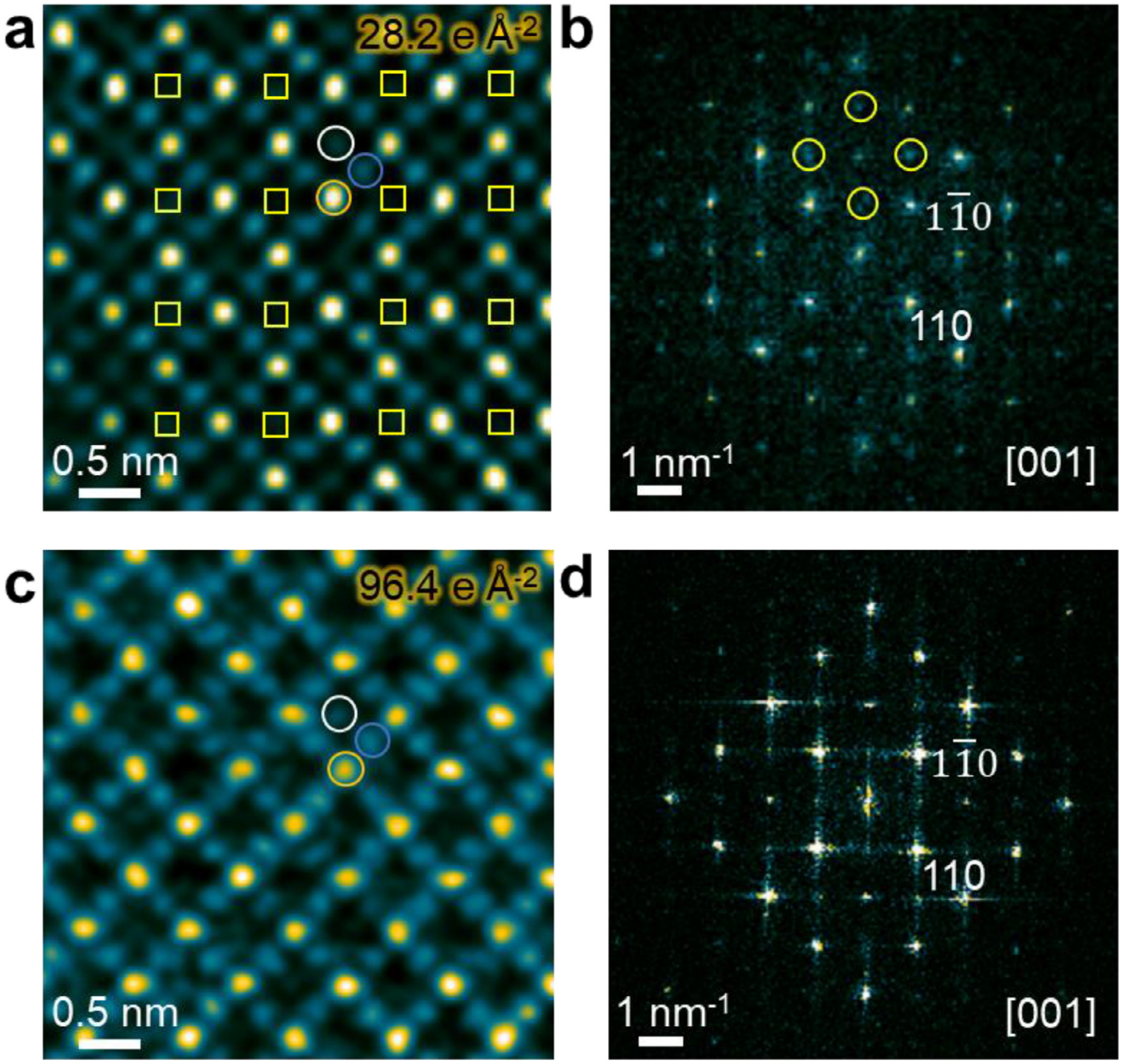

Fig. 2. Low-dose imaging of the atomic structure of $MAPbI_3$. a HRTEM image of nanocrystal $MAPbI_3$ at a dose of 28.2 e $Å^{-2}$ by using a direct-detection electron-counting camera. The yellow circle shows the Pb^{2+}/I^- columns, the blue circle shows pure I^- columns and the white circle shows the MA^+ columns. The yellow squares indicate the MA^+vacancies. b The corresponding FFT pattern along the [001] direction. The yellow circles mark the superstructure diffraction spots. c Filtered STEM image of $MAPbI_3$ film directly grown on the ultrathin carbon-coated TEM grid at a dose of 96.4 e $Å^{-2}$. The original STEM image is shown in Fig. S12a. The yellow, blue, and white circles represent Pb^{2+}/I^-, I^-, and MA^+ columns. d The corresponding FFT pattern along the [001] direction.

cies can be identified while some columns belonging to MA^+ show increased intensity (as shown by the blue arrow in Fig. S4) likely due to the diffusion of I^- and Pb^{2+} to the columns of MA^+ [43]. This suggests the obtained structure might suffer from beam damage with higher-order diffraction spots lost (Fig. 2d). However, it is difficult to quantify the content of MA^+ vacancies due to the low intensity of MA^+ as well as the diffusion of I^- and Pb^{2+} to the columns of MA^+. In addition, the MA^+ is light while the I^- and Pb^{2+} are heavy and the very different mass causes significantly different dechanneling effect, making the quantification even more challenging. With the increased electron dose, $MAPbI_3$ gradually decomposes into PbI_2 within 500.0 e $Å^{-2}$ (Fig. S5). For both of these two imaging techniques, MA^+ vacancies are inevitably generated even at a relatively low dose that is necessary for decent atomic structure visualization. The contrast of TEM images highly depends on the thickness of the sample and the imaging defocus and thus is less reliable to identify specific atomic columns, while the contrast of STEM images is easy to interpret and sensitive to the atomic number (Z). Accordingly, we adopt STEM techniques to characterize the atomic structures of the defects in $MAPbI_3$.

Fig. 3a is a STEM image of the $MAPbI_3$ along the [001] direction. Some boundaries are indicated by the white lines. These boundaries prefer to lie along the [100] and [010] directions. Since the contrast of STEM images is sensitive to Z, each type of the atomic column can be identified as indicated in magnified Fig. 3b. Note that MA^+ vacancies are formed due to the beam damage while the same structure without MA^+ is verified to be unstable (Fig. S6), thus the atomic model of the boundary before forming MA^+ vacancies is proposed in Fig. 3c,d. The structure transition from pristine $MAPbI_3$ (Fig. 3c) to the boundary structure (Fig. 3d) can be achieved as follows: the right region with green octahedrons shifts a half of the unit cell along the [100]/[010] direction, accompanied by the corner-sharing $[PbI_6]^{4-}$ octahedron transforming into edge-shared one. Indeed, this is a typical feature of the APB. Since electron beam usually leads to the formation of vacancies and local ion migration [25,27,43], such a collective shift of atomic columns in APB should be the pristine feature of $MAPbI_3$ rather than induced by the electron beam illumination. The DFT-optimized atomic structure of APB is shown in Fig. S7 and the formation energy of such APB is calculated to be 0.8 eV per unit, indicating APB is easy to form during the synthesis process.

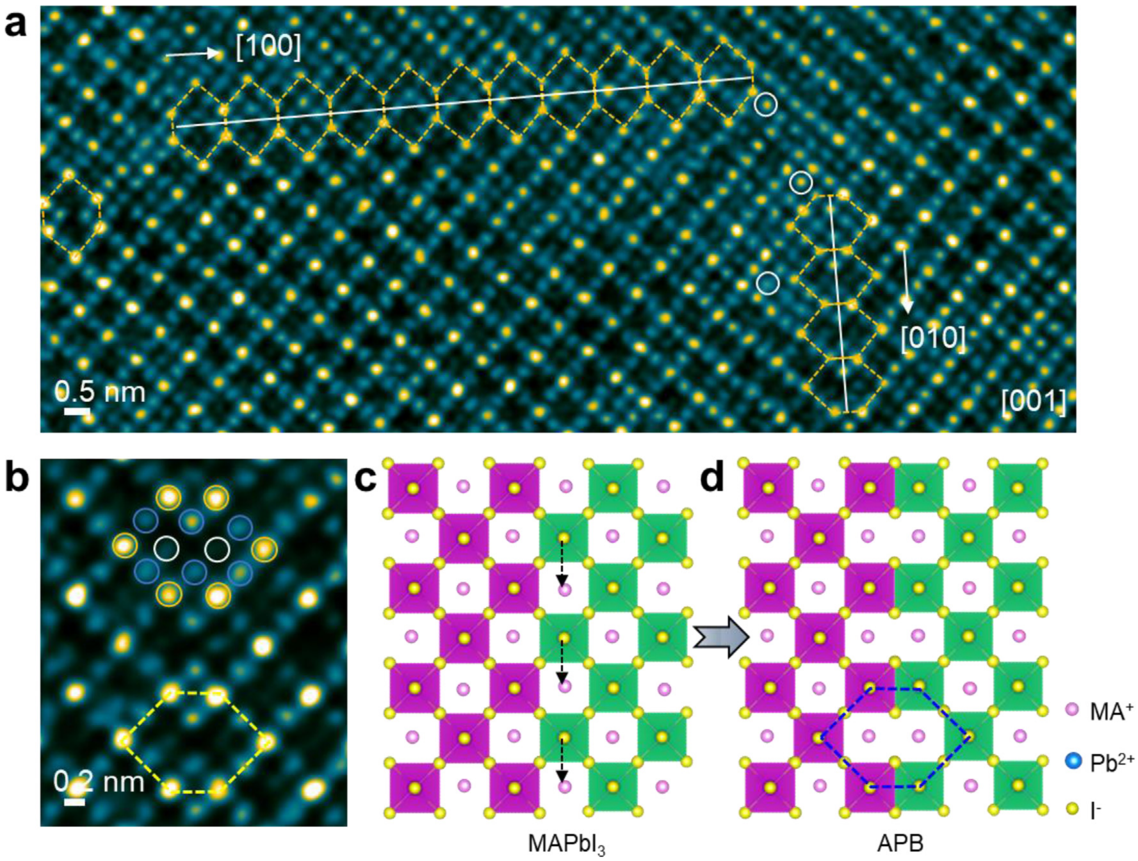

Fig. 3. Atomic structure of antiphase boundary in $MAPbI_3$. a Atomic structure of APB along the [001] direction. The white lines highlight that APB prefers to lie along the [100] and [010] directions. b Enlarged view of the atomic structure of APB. The yellow, blue, and white circles indicate Pb^{2+}/I^-, I^-, and MA^+ columns, respectively. Fig. a and b have been filtered and the original STEM images are shown in Fig. S12 b and c. c Atomic model of $MAPbI_3$. The $[PbI_6]^{4-}$ octahedrons are highlighted by the purple (left region) and green color (right region). d Atomic model of APB in $MAPbI_3$. After green octahedrons in $MAPbI_3$ shifts a half of the unit cell along the a/b direction, as the black arrows indicate, the structure transforms into APB. The corner-sharing octahedrons become edge-shared ones. The blue hexagon in d corresponds to the yellow one in a and b. Pink, blue, and yellow balls indicate MA^+, Pb^{2+}, and I^- respectively.

More representative STEM images of the APB defect in $MAPbI_3$ are shown in Fig. S8. The line length of APB ranges from 3 nm to 10 nm. Based on the total line length of these APB in one grain (71.1 nm) and the corresponding area (2.67×10^3 nm^2), the density of APB, defined as the line length of APB per unit area [44], is estimated to be 26.4 μm^{-1}. Considering we have not scanned the whole grain of the film, it is likely the line length of APB in one whole grain is also 71.1 nm, leading to a minimum APB density of 1.4 μm^{-1} with an average area of one grain at 5.06×10^4 nm^2 (Fig. S1b). Thus the density of APB defects is roughly estimated to range from 1.4 to 26.4 μm^{-1}, which shows a similar magnitude to that reported in GaAs [44]. Moreover, such APB structures have also been observed in all-inorganic perovskite (e.g. $CsPbBr_3$). Fig. 4a is the atomic-scale STEM image of orthogonal $CsPbBr_3$ along the [110] direction judging from the corresponding FFT pattern (Fig. 4b). Yellow, blue and white circles in Fig. 4a indicate the Pb^{2+}/Br^-, Br^-, and Cs^+ columns. Based on the enlarged image in Fig. 4c, the atomic structure of such APB structure can be identified (Fig. 4d), which is similar to that observed in $MAPbI_3$, suggesting such an APB defect is general in OIHPs and its all-inorganic counterpart. Note that such an APB structure is a 90° boundary, which is difficult to identify by electron diffraction or FFT patterns without atomic-scale imaging. Indeed, most previous electron microscopy studies failed to observe them, without which the effect on the material performance is impossible to establish.

Having obtained the atomic structure of APB, we are now ready to investigate how such an APB influences the electrical properties by DFT calculations. Fig. 5a shows the density of state (DOS) of $MAPbI_3$ and APB. It is observed that the APB does not introduce any deep-level defects within the bandgap, which usually prevents charge transport and facilitates the nonradiative recombination. To reveal its effect on the electron and hole transport, we further examined the band diagram across the APB. Fig. 5b presents a layer-by-layer projection of the DOS (LDOS) across the APB. A large bandgap offset can be observed across the APB. Specifically, the conduction band minimum (CBM) offsets +31 meV while the valence band maximum (VBM) offsets −41 meV at the APB, thus APB features a type-I band alignment, which efficiently repels both electrons and holes [45]. This result is consistent with the charge density of the CBM and VBM of APB as shown in Fig. 5c-f. It is observed that the evenly-distributed charge density of CBM and VBM in the bulk $MAPbI_3$ decreases at the APB since the positive offset of CBM repels away electrons from APB and the negative offset of VBM also drives the holes away from it.

It is also desirable to clarify the influence of APB on ion migration, which is significant for PSCs. Previous studies show that MA^+ and I^- are easy to migrate within MAPbI3 while the diffusion barrier of Pb2$^+$ is higher [46], which can be induced by high temperatures [47]. By DFT calculations, we have compared the diffusion barriers of MA^+, Pb^{2+}, and I^- at the APB to those in the bulk under a similar diffusion pathway for each ion as shown in Fig. 6. Fig. 6a and Fig. 6b show the schematic diagram of vacancy-mediated migration pathways of these ions in the bulk and at the APB. Specifically, MA^+ diffuses to the neighbouring vacant A-site while Pb^{2+} migrates along the diagonal of the (110) plane through Pb^{2+} vacancy and I^- migrates along an edge of the octahedron, as illus-

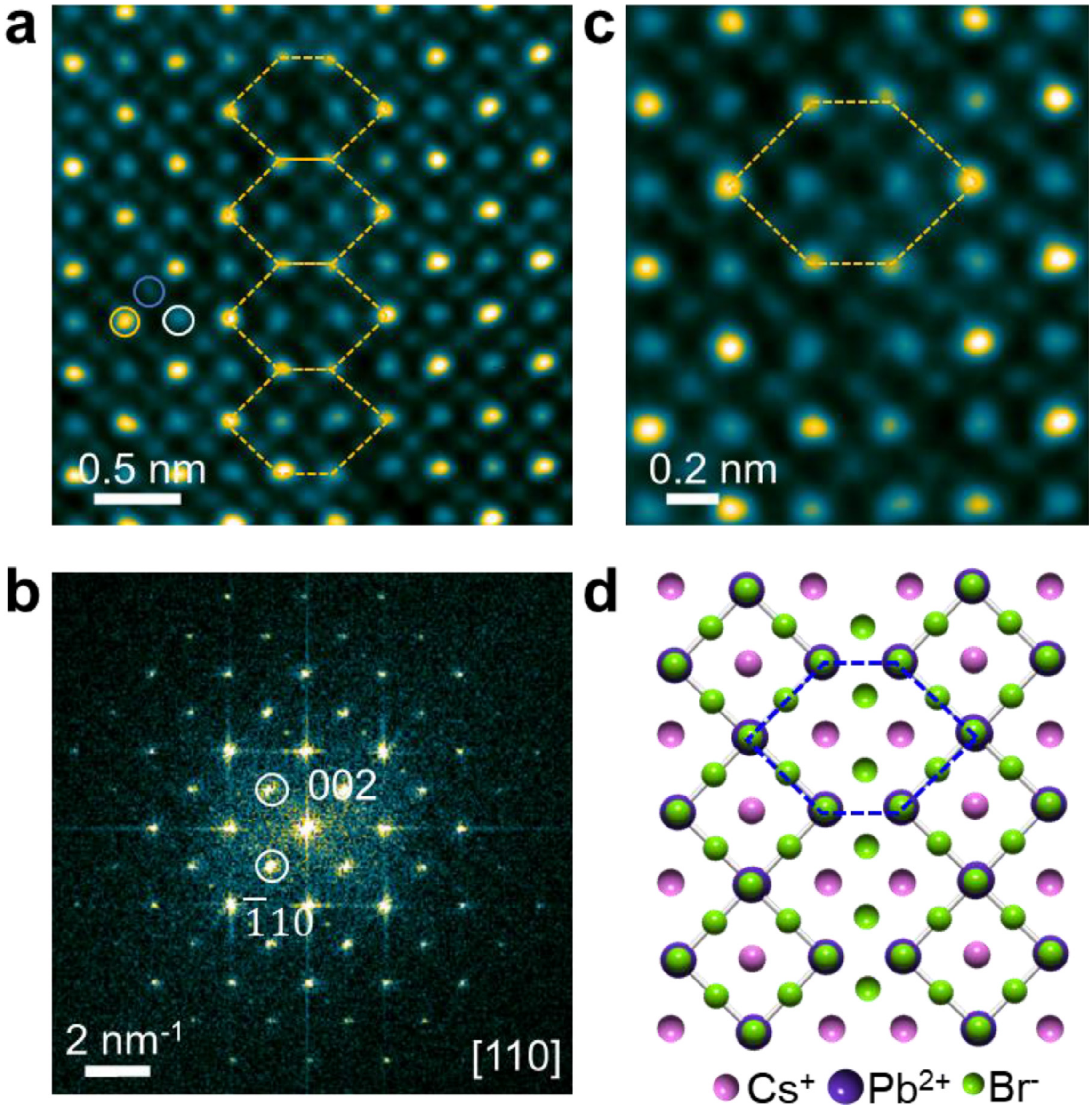

Fig. 4. Atomic structure of APB in $CsPbBr_3$. a, c Atomic-scale STEM image of APB in $CsPbBr_3$. Yellow, blue and white circles indicate the Pb^{2+}/Br^-, Br^-, and Cs^+ columns. b The corresponding FFT pattern along the [110] direction of orthogonal $CsPbBr_3$. d Atomistic configuration of the APB structure in $CsPbBr_3$. Pink, purple, and orange balls represent Cs^+, Pb^{2+}/Br^-, and Br^- columns, respectively. These STEM images have been filtered using Gaussian blur after stacking with 5 images. The original images were shown in Fig. S13.

trated in Fig. S9. Fig. 6c and Table S2 present the diffusion barriers of MA^+, Pb^{2+}, and I^- along the corresponding pathways. The diffusion barriers in the bulk $MAPbI_3$ for MA^+, Pb^{2+}, and I^- is 0.98, 2.37, and 0.55 eV, similar to the reported values [46] while the diffusion barrier of MA^+, Pb^{2+}, and I^- decreases to 0.77, 1.38 and 0.43 eV at the APB. This suggests MA^+, Pb^{2+}, and I^- are easier to migrate along with the APB, which serves as a fast ion-diffusion channel and likely causes a more facile decomposition of MAPbI3. As shown in Fig. S10, $MAPbI_3$ with APB structures decomposes into PbI_2 within 385.6 e Å-2, which is lower than that of the bulk MAPbI3 (500 e Å-2).

The intrinsic optoelectronic properties of OIHPs are greatly influenced by the defects within the crystal [6,48]. To fabricate high-performance PSCs, it is necessary to enhance the understanding of defects in OIHPs. The frequently-used techniques to characterize the defects like steady-state photoluminescence [49], space charge limited current [50], and thermally simulated current [51] can provide useful information about defects, but they are unable to identify the specific types of defects as well as their atomic structures. Accordingly TEM-based techniques have been widely used to reveal the structural defects of halide perovskites at multiple scales [18,28,52-54]. However, due to the extreme beam sensitivity of OIHPs, chemical and structural changes occur during TEM characterizations, especially for high-dose techniques like conventional HRTEM, energy dispersive spectroscopy, EELS and in situ TEM techniques [55]. For example, the electron beam illumination is reported to induce the continuous phase transition from $MAPbI_3$ to PbI_2 while most researches failed to notice such degradation and mistakenly identified PbI_2 as $MAPbI_3$ [25,40]. Besides, considering the large doses during in situ TEM study of OIHPs [47], the electron-beam-induced damage possibly contributes a lot to the observed phenomena. Thus the low dose imaging technique is of great importance to reveal the intrinsic structural features of OIHPs.

To decrease the electron beam damage, we adopted low-dose TEM imaging techniques. A previous study has observed the APB

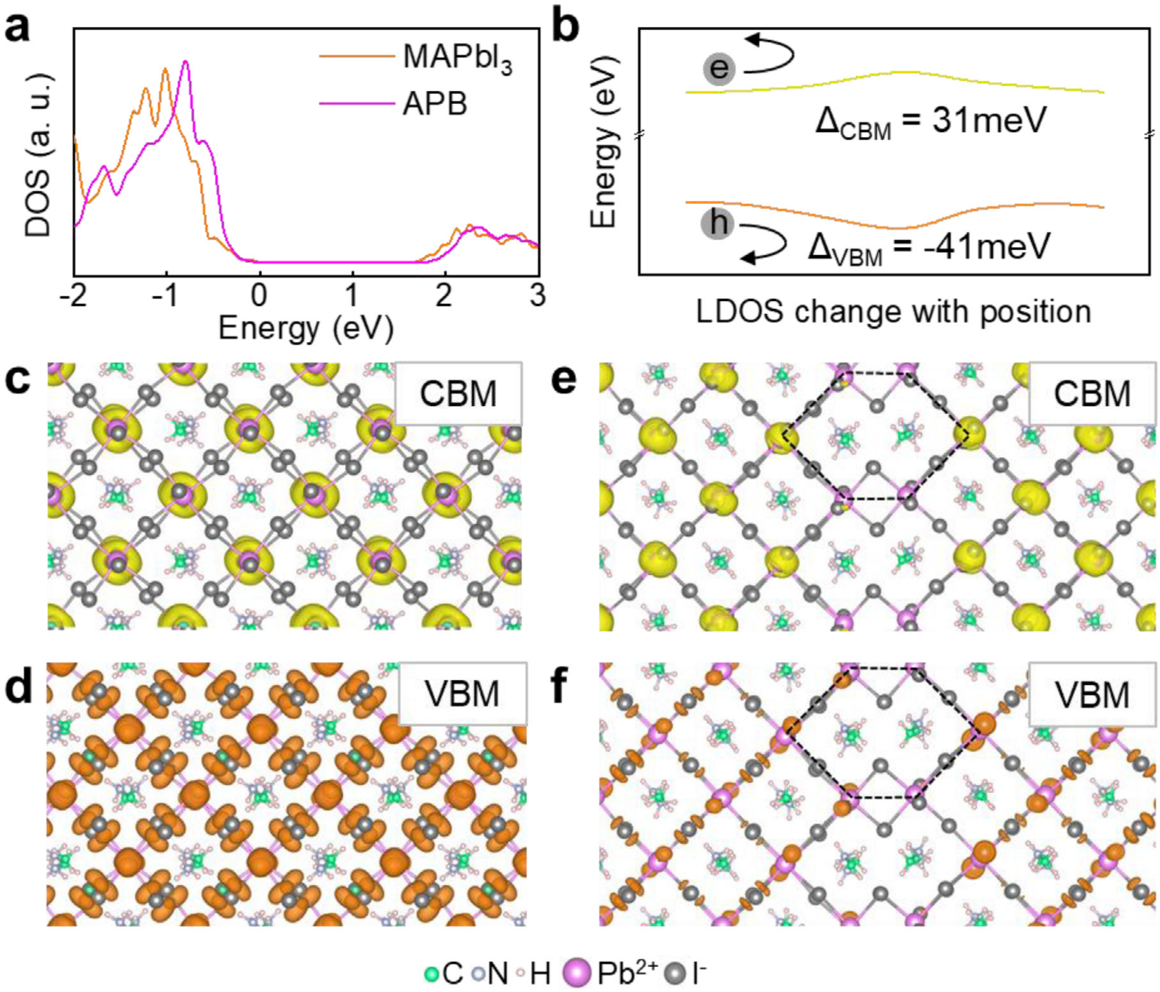

Fig. 5. The effect of APB on electrical properties. a The DOS of the bulk $MAPbI_3$ and APB defect. b LDOS and band diagram of APB with a positive offset (31 meV) of the conduction band and a negative offset (−41 meV) of the valance band, thus repelling both electrons and holes. c, d Charge density of CBM and VBM of the bulk $MAPbI_3$. e, f Charge density of CBM and VBM of the APB defect.

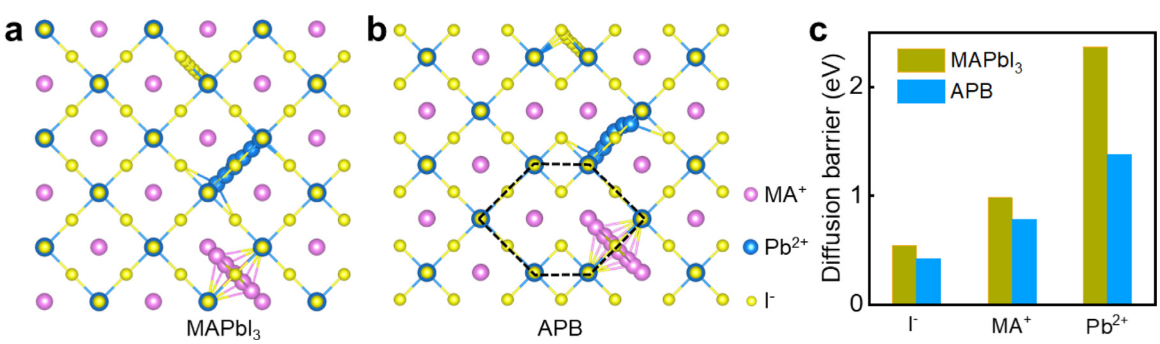

Fig. 6. The effect of APB on ion migration. a, b Schematic diagram to illustrate the migration pathway of MA^+, Pb^{2+}, and I^- in the bulk $MAPbI_3$ and at the APB. Pink, blue, and yellow balls indicate MA^+, Pb^{2+}, and I^- respectively. The diffusion pathway for each ion in the bulk $MAPbI_3$ and at the APB is chosen to be similar for a better comparison of the migration barrier. The specific pathway in the optimized structure can be found in Fig. S9. c The diffusion barriers of MA^+, Pb^{2+}, and I^- along the corresponding diffusion pathways in a and b at the APB and in the bulk $MAPbI_3$. The diffusion barriers have also been listed in Table S2.

in $FAPbI_3$, though the elaborate atomic-scale configuration is still unknown [27]. By using low dose STEM techniques, we directly observed the existence of APB in $MAPbI_3$ and resolved its atomic structure. Based on the identified atomic-scale configuration of APB, we further clarified its influence on the electrical and ionic activities of OIHPs with the assistance of DFT calculations, contributing to an improved understanding on the relationship between defect structures and properties. In traditional semiconductors, planar defects usually introduce deep-level defects within the bandgap, hindering the charges transport and facilitating the non-radiative recombination [18]. In contrast, our work reveals that the planar defect of APB in $MAPbI_3$ does not introduce any deep-level defects within the bandgap. Moreover, such APB repels the electrons and holes and features a type-I band alignment. It has been reported that such type-I band alignment at the grain boundaries on the surface of OIHPs can effectively repel carriers and return them to the inside of the grain, thus decreasing the carrier loss and facilitating an improved optoelectronic performance [45,56]. The APB observed in our work is mainly inside the grain, and thus delicate engineering is necessary to control its distribution.

Furthermore, ion migration is regarded as one of the most important issues in PSCs, responsible for phase segregation, J-V hysteresis, and device degradation [57]. Such ion migration can be intrinsic due to the low migration energy. Our work finds that the APB provides additional ion diffusion channels and the diffusion barrier of MA^+, Pb^{2+}, and I^- decreases by 21.8%, 41.8%, and 20.4% respectively at the APB. Such a low diffusion barrier induces easier ion migration and greatly increases the chemical activity of $MAPbI_3$, leading to more facile structure degradation (Fig. S10) that destroys long-term operational stabilities [58]. In particular, the decrease of the diffusion barrier for Pb^{2+} from 2.37 to 1.38 eV makes it easier for Pb^{2+} to diffusion, as indicated by Pb^{2+} vacancies (Fig. S11) and the increased intensity at the columns belonging to MA^+ (highlighted by the circles in Fig. 3a). The diffusion of Pb^{2+} can form Pb^{2+} interstitials and Pb^{2+}-related antistites, both of which can create deep-level defect traps as recombination centers [7] and are detrimental to efficient charge extractions. These findings suggest efficient control and engineering of defects are highly desirable for high-performance PSCs. For example, reducing the density of the twin boundaries in $MA_{1-x}FA_xPbI_3$ via defect-engineering [5] and minimizing hydrogen vacancies [59] enables much-improved performance of PSCs.

4. Conclusions

In summary, by using low dose STEM techniques, we have successfully observed the existence of APB in OIHPs, revealed its atomic structure, and further clarified its impact on electronic structure, ion migration, and structure instabilities. Atomic-resolution STEM images show that the APB consists of edge-sharing $[PbI_6]^{4-}$ octahedron and lies along the [100] and [010] directions. Further DFT calculations based on the identified atomic-scale configuration show that the APB repels both electrons and holes and facilitates fast diffusion of MA^+, Pb^{2+}, and I^-. The fast ion diffusion at the APB further leads to a quick decomposition into PbI_2. These findings enhance a better understanding of the relationships between structures and optoelectronic properties of OIHPs and suggest that controlling the APB is essential for their stability.

Declaration of Competing Interest

The authors declare no conflict of interest.

Acknowledgements

This research was financially supported by the National Natural Science Foundation of China (52125307, 11974023, 52021006, 11772207, 22003074, 52072006), Youth Innovation Promotion Association CAS, the Key R&D Program of Guangdong Province (2018B030327001, 2018B010109009), the Guangdong Provincial Key Laboratory Program from the Department of Science and Technology of Guangdong Province (2021B1212040001), Guangdong Basic and Applied Basic Research Foundation (2020A1515110580), International Cooperation Project of Guangdong Province (No. 2019A050510049), Guangdong Basic and Applied Basic Research Foundation (2022A1515012463), SIAT Innovation Program for Excellent Young Researchers (2022**), Natural Science Foundation of Hebei Province for distinguished young scholar (A2019210204) and China Postdoctoral Science Foundation (2021M703391). The authors gratefully acknowledge the Electron Microscopy Laboratory at Peking University for the use of electron microscopes and the support of the Center for Computational Science and Engineering at Southern University of Science and Technology.

Author contributions

P. Gao, J.Y. Li, and S.L. Chen conceived and supervised the project. S.L. Chen carried out TEM experiments and analysed experimental data with the direction of P. Gao and help from J.M. Zhang. C.W. Wu performed the calculations under the guidance of X. Wang. Q.Y. Shang synthesized $MAPbI_3$ thin films under the direction of Q. Zhang. Z.T. Liu carried out the EELS measurements. C.L. He prepared the $CsPbBr_3$ materials under the guidance of J.J. Zhao. W.K. Zhou and J.L. Qi provided additional specimens. S.L. Chen, J.Y. Li, and P. Gao wrote the manuscript and all authors participated in the revisions.

Supplementary materials

Supplementary material associated with this article can be found, in the online version, at doi:10.1016/j.actamat.2022.118010.

References

[1] A. Kojima, K. Teshima, Y. Shirai, T. Miyasaka, Organometal halide perovskites as visible-light sensitizers for photovoltaic cells, J. Am. Chem. Soc. 131 (2009) 6050.
[2] X. Zheng, Y. Hou, C. Bao, J. Yin, F. Yuan, Z. Huang, K. Song, J. Liu, J. Troughton, N. Gasparini, C. Zhou, Y. Lin, D. Xue, B. Chen, A.K. Johnston, N. Wei, M.N. Hedhili, M. Wei, A.Y. Alsalloum, P. Maity, B. Turedi, C. Yang, D. Baran, T.D. Anthopoulos, Y. Han, Z. Lu, O.F. Mohammed, F. Gao, E.H. Sargent, O.M. Bakr, Managing grains and interfaces via ligand anchoring enables 22.3%-efficiency inverted perovskite solar cells, Nat. Energy 5 (2020) 131.
[3] W. Chen, Y. Wu, Y. Yue, J. Liu, W. Zhang, X. Yang, H. Chen, E. Bi, I. Ashraful, M. Grätzel, L. Han, Efficient and stable large-area perovskite solar cells with inorganic charge extraction layers, Science 350 (2015) 944.
[4] T. Doherty, S. Nagane, D.J. Kubicki, Y.K. Jung, D.N. Johnstone, A.N. Iqbal, D. Guo, K. Frohna, M. Danaie, E.M. Tennyson, S. Macpherson, A. Abfalterer, M. Anaya, Y.H. Chiang, P. Crout, F.S. Ruggeri, S. Collins, C.P. Grey, A. Walsh, P.A. Midgley, S.D. Stranks, Stabilized tilted-octahedra halide perovskites inhibit local formation of performance-limiting phases, Science 374 (2021) 1598.
[5] W. Li, M.U. Rothmann, Y. Zhu, W. Chen, C. Yang, Y. Yuan, Y.Y. Choo, X. Wen, Y. Cheng, U. Bach, J. Etheridge, The critical role of composition-dependent intragrain planar defects in the performance of $MA_{1-x}FA_xPbI_3$ perovskite solar cells, Nat. Energy 6 (2021) 624.
[6] C. Ran, J. Xu, W. Gao, C. Huang, S. Dou, Defects in metal triiodide perovskite materials towards high-performance solar cells: origin, impact, characterization, and engineering, Chem. Soc. Rev. 47 (2018) 4581.
[7] W. Yin, T. Shi, Y. Yan, Unique properties of halide perovskites as possible origins of the superior solar cell performance, Adv. Mater. 26 (2014) 4653.
[8] D.W. de Quilettes, S.M. Vorpahl, S.D. Stranks, H. Nagaoka, G.E. Eperon, M.E. Ziffer, H.J. Snaith, D.S. Ginger, Impact of microstructure on local carrier lifetime in perovskite solar cells, Science 348 (2015) 683.
[9] Y. Yuan, J. Huang, Ion migration in organometal trihalide perovskite and its impact on photovoltaic efficiency and stability, Acc. Chem. Res. 49 (2016) 286.
[10] Y. Shao, Y. Fang, T. Li, Q. Wang, Q. Dong, Y. Deng, Y. Yuan, H. Wei, M. Wang, A. Gruverman, J. Shield, J. Huang, Univ. Of Nebraska-Lincoln LNUS. Grain boundary dominated ion migration in polycrystalline organic-inorganic halide perovskite films, Energy Environ. Sci. 9 (2016) 1752.
[11] J.S. Yun, A. Ho-Baillie, S. Huang, S.H. Woo, Y. Heo, J. Seidel, F. Huang, Y. Cheng, M.A. Green, Benefit of grain boundaries in organic-inorganic halide planar perovskite solar cells, J. Phys. Chem. Lett. 6 (2015) 875.
[12] Y. Wang, W. Fang, R. Long, O.V. Prezhdo, Symmetry breaking at $MAPbI_3$ perovskite grain boundaries suppresses charge recombination: time-domain ab initio analysis, J. Phys. Chem. Lett. 10 (2019) 1617.
[13] B.D. Esser, A.J. Hauser, R.E.A. Williams, L.J. Allen, P.M. Woodward, F.Y. Yang, D.W. McComb, Quantitative STEM imaging of order-disorder phenomena in double perovskite thin films, Phys. Rev. Lett. 117 (2016) 176101.
[14] Y. Murakami, K. Niitsu, T. Tanigaki, R. Kainuma, H.S. Park, D. Shindo, Magnetization amplified by structural disorder within nanometre-scale interface region, Nat. Commun. 5 (2014) 4133.
[15] T. Choi, Y. Horibe, H.T. Yi, Y.J. Choi, W. Wu, S.W. Cheong, Insulating interlocked ferroelectric and structural antiphase domain walls in multiferroic $YMnO_3$, Nat. Mater. 9 (2010) 253.
[16] H. Liu, H. Wu, K.P. Ong, T. Yang, P. Yang, P.K. Das, X. Chi, Y. Zhang, C. Diao, W.K.A Wong, Giant piezoelectricity in oxide thin films with nanopillar structure, Science 369 (2020) 292.
[17] J.H. Kim, S.Y. Kim, S.O. Park, G.Y. Jung, S. Song, A. Sohn, S.W. Kim, S.K. Kwak, S.Y. Kwon, Z. Lee, Antiphase boundaries as faceted metallic wires in 2D transition metal dichalcogenides, Adv. Sci. 7 (2020) 2000788.

[18] A.S. Thind, G. Luo, J.A. Hachtel, M.V. Morrell, S.B. Cho, A.Y. Borisevich, J.C. Idrobo, Y. Xing, R. Mishra, Atomic structure and electrical activity of grain boundaries and ruddlesden-popper faults in cesium lead bromide perovskite, Adv. Mater. 31 (2019) 1805047.
[19] S. Tong, J. Wang, C. Wu, C. Wu, J. Chang, P. Wei, The reduction of antiphase boundary defects by the surfactant antimony and its application to the III–V multi-junction solar cells, Sol. Energy Mater Sol. Cells 144 (2016) 418.
[20] J.L. Kaufman, A. Van Der Ven, Antiphase boundary migration as a diffusion mechanism in a P3 sodium layered oxide, Phys. Rev. Mater. 5 (2021) 055401.
[21] G. Hasegawa, N. Kuwata, Y. Tanaka, T. Miyazaki, N. Ishigaki, K. Takada, J. Kawamura, Tracer diffusion coefficients of Li^+ ions in *c*-axis oriented Li_xCoO_2 thin films measured by secondary ion mass spectrometry, Phys. Chem. Chem. Phys. 23 (2021) 2438.
[22] T. Heisig, J. Kler, H. Du, C. Baeumer, F. Hensling, M. Glöß, M. Moors, A. Locatelli, T.O. Menteş, F. Genuzio, J. Mayer, R.A. De Souza, R. Dittmann, Antiphase boundaries constitute fast cation diffusion paths in $SrTiO_3$ memristive devices, Adv. Funct. Mater. 30 (2020) 2004118.
[23] F.V.E. Hensling, H. Du, N. Raab, C. Jia, J. Mayer, R. Dittmann, Engineering antiphase boundaries in epitaxial $SrTiO_3$ to achieve forming free memristive devices, APL Mater. 7 (2019) 101127.
[24] D.B. Holt, Antiphase boundaries in semiconducting compounds, J. Phys. Chem. Solids 30 (1969) 1297.
[25] S. Chen, X. Zhang, J. Zhao, Y. Zhang, G. Kong, Q. Li, N. Li, Y. Yu, N. Xu, J. Zhang, K. Liu, Q. Zhao, J. Cao, J. Feng, X. Li, J. Qi, D. Yu, J. Li, P Gao, Atomic scale insights into structure instability and decomposition pathway of methylammonium lead iodide perovskite, Nat. Commun. 9 (2018) 4807.
[26] D. Zhang, Y. Zhu, L. Liu, X. Ying, C. Hsiung, R. Sougrat, K. Li, Y. Han, Atomic-resolution transmission electron microscopy of electron beam-sensitive crystalline materials, Science 359 (2018) 675.
[27] M.U. Rothmann, J.S. Kim, J. Borchert, K.B. Lohmann, C.M. O'Leary, A.A. Sheader, L. Clark, H.J. Snaith, M.B. Johnston, P.D. Nellist, L.M. Herz, Atomic-scale microstructure of metal halide perovskite, Science 370 (2020) 548.
[28] M.U. Rothmann, W. Li, Y. Zhu, U. Bach, L. Spiccia, J. Etheridge, Y. Cheng, Direct observation of intrinsic twin domains in tetragonal $CH_3NH_3PbI_3$, Nat. Commun. 8 (2017) 14547.
[29] Y. Liang, Q. Shang, M. Li, S. Zhang, X. Liu, Q. Zhang, Solvent recrystallization-enabled green amplified spontaneous emissions with an ultra-low threshold from pinhole-free perovskite films, Adv. Funct. Mater. 31 (2021) 2106108.
[30] X. Li, Y. Wu, S. Zhang, B. Cai, Y. Gu, J. Song, H. Zeng, $CsPbX_3$ quantum dots for lighting and displays: room-temperature synthesis, photoluminescence superiorities, underlying origins and white light-emitting diodes, Adv. Funct. Mater. 26 (2016) 2435.
[31] J. Gonnissen, A. De Backer, A.J. den Dekker, G.T. Martinez, A. Rosenauer, J. Sijbers, S. Van Aert, Optimal experimental design for the detection of light atoms from high-resolution scanning transmission electron microscopy images, Appl. Phys. Lett. 105 (2014) 63116.
[32] A.C. Johnston-Peck, J.S. DuChene, A.D. Roberts, W.D. Wei, A.A. Herzing, Dose-rate-dependent damage of cerium dioxide in the scanning transmission electron microscope, Ultramicroscopy 170 (2016) 1.
[33] G. Kresse, J. Hafner, Ab initio molecular dynamics for open-shell transition metals, Phys. Rev. B 48 (1993) 13115.
[34] A.N.S.M. Kozlov, F. Viñes, F. Illas, Electronic-structure-based chemical descriptors:(in) dependence on self-interaction and Hartree-Fock exchange, Phys. Rev. B 54 (1996) 11169.
[35] P.E. Blöchl, Projector augmented-wave method, Phys. Rev. B 50 (1994) 17953.
[36] J. Furthmüller, G. Kresse, Efficient iterative schemes for ab initio total-energy calculations using a plane-wave basis set, Phys. Rev. B 54 (1996) 11169.
[37] S. Grimme, J. Antony, S. Ehrlich, H Krieg, A consistent and accurate ab initio parametrization of density functional dispersion correction (DFT-D) for the 94 elements H-Pu, J. Chem. Phys. 132 (2010) 154104.
[38] H.J. Monkhorst, J.D. Pack, Special points for Brillouin-zone integrations, Phys. Rev. B 13 (1976) 5188.
[39] G. Henkelman, B.P. Uberuaga, H. Jónsson, A climbing image nudged elastic band method for finding saddle points and minimum energy paths, J. Chem. Phys. 113 (2000) 9901.
[40] S. Chen, P. Gao, Challenges, myths, and opportunities of electron microscopy on halide perovskites, J. Appl. Phys. 128 (2020) 10901.
[41] S. Chen, Y. Zhang, J. Zhao, Z. Mi, J. Zhang, J. Cao, J. Feng, G. Zhang, J. Qi, J. Li, P. Gao, Transmission electron microscopy of organic-inorganic hybrid perovskites: myths and truths, Sci. Bull. 65 (2020) 1643.
[42] Y. Li, W. Zhou, Y. Li, W. Huang, Z. Zhang, G. Chen, H. Wang, G. Wu, N. Rolston, R. Vila, W. Chiu, Y. Cui, Unravelling degradation mechanisms and atomic structure of organic-inorganic halide perovskites by cryo-EM, Joule 3 (2019) 2854.
[43] S. Chen, C. Wu, B. Han, Z. Liu, Z. Mi, W. Hao, J. Zhao, X. Wang, Q. Zhang, K. Liu, J. Qi, J. Cao, J. Feng, D. Yu, J. Li, P. Gao, Atomic-scale imaging of $CH_3NH_3PbI_3$ structure and its decomposition pathway, Nat. Commun. 12 (2021) 5516.
[44] C. Barrett, A.G. Lind, X. Bao, Z. Ye, K.Y. Ban, P. Martin, E. Sanchez, Y. Xin, K.S. Jones, Quantitative correlation of interfacial contamination and antiphase domain boundary density in GaAs on Si (100), J. Mater. Sci. 51 (2016) 449.
[45] Q. Chen, H. Zhou, T. Song, S. Luo, Z. Hong, H. Duan, L. Dou, Y. Liu, Y. Yang, Controllable self-induced passivation of hybrid lead iodide perovskites toward high performance solar cells, Nano Lett. 14 (2014) 4158.
[46] C. Eames, J.M. Frost, P.R.F. Barnes, B.C. O Regan, A. Walsh, M.S Islam, Ionic transport in hybrid lead iodide perovskite solar cells, Nat. Commun. 6 (2015) 7497.
[47] G. Divitini, S. Cacovich, F. Matteocci, L. Cinà, A. Di Carlo, C. Ducati, In situ observation of heat-induced degradation of perovskite solar cells, Nat. Energy 1 (2016) 15012.
[48] Z. Ni, H. Jiao, C. Fei, H. Gu, S. Xu, Z. Yu, G. Yang, Y. Deng, Q. Jiang, Y. Liu, Y. Yan, J. Huang, Evolution of defects during the degradation of metal halide perovskite solar cells under reverse bias and illumination, Nat. Energy 7 (2021) 65.
[49] G. Xing, N. Mathews, S.S. Lim, N. Yantara, X. Liu, D. Sabba, M. Grätzel, S. Mhaisalkar, T.C. Sum, Low-temperature solution-processed wavelength-tunable perovskites for lasing, Nat. Mater. 13 (2014) 476.
[50] D. Shi, V. Adinolfi, R. Comin, M. Yuan, E. Alarousu, A. Buin, Y. Chen, S. Hoogland, A. Rothenberger, K. Katsiev, Y. Losovyj, X. Zhang, P.A. Dowben, O.F. Mohammed, E.H. Sargent, O.M. Bakr, Solar cells. Low trap-state density and long carrier diffusion in organolead trihalide perovskite single crystals, Science 347 (2015) 519.
[51] Y. Shao, Z. Xiao, C. Bi, Y. Yuan, J. Huang, Origin and elimination of photocurrent hysteresis by fullerene passivation in $CH_3NH_3PbI_3$ planar heterojunction solar cells, Nat. Commun. 5 (2014) 5784.
[52] Y. Yu, D. Zhang, P. Yang, Ruddlesden-popper phase in two-dimensional inorganic halide perovskites: a plausible model and the supporting observations, Nano Lett. 17 (2017) 5489.
[53] J. Liu, K. Song, Y. Shin, X. Liu, J. Chen, K.X. Yao, J. Pan, C. Yang, J. Yin, L. Xu, Light-induced self-assembly of cubic $CsPbBr_3$ perovskite nanocrystals into nanowires, Chem. Mater. 31 (2019) 6642.
[54] S. Cai, J. Dai, Z. Shao, M.U. Rothmann, Y. Jia, C. Gao, M. Hao, S. Pang, P. Wang, S.P Lau, Atomically resolved electrically active intragrain interfaces in perovskite semiconductors, J. Am. Chem. Soc. 144 (2022) 1910.
[55] Y. Zhou, H. Sternlicht, N.P. Padture, Transmission electron microscopy of halide perovskite materials and devices, Joule 3 (2019) 641.
[56] C. Luo, Y. Zhao, X. Wang, F. Gao, Q Zhao, Self-induced type-I band alignment at surface grain boundaries for highly efficient and stable perovskite solar cells, Adv. Mater. 33 (2021) 2103231.
[57] T. Zhang, C. Hu, S. Yang, Ion migration: a "double-edged sword" for halide-perovskite-based electronic devices, Small Methods 4 (2020) 1900552.
[58] W. Chen, Z. Gan, M.A. Green, B. Jia, X. Wen, Revealing dynamic effects of mobile ions in halide perovskite solar cells using time-resolved microspectroscopy, Small Methods 5 (2021) 2000731.
[59] X. Zhang, J. Shen, M.E. Turiansky, C.G Van de Walle, Minimizing hydrogen vacancies to enable highly efficient hybrid perovskites, Nat. Mater. 20 (2021) 971.